



THE UNIVERSITY *of* EDINBURGH

Edinburgh Research Explorer

Uplift and Seismicity driven by Magmatic Inflation at Sierra Negra Volcano, Galápagos Islands

Citation for published version:

Bell, A, Hernandez, S, LaFemina, PC & Ruiz, M 2021, 'Uplift and Seismicity driven by Magmatic Inflation at Sierra Negra Volcano, Galápagos Islands', *Journal of Geophysical Research. Solid Earth*, vol. 126, no. 7, e2021JB022244. <https://doi.org/10.1029/2021JB022244>

Digital Object Identifier (DOI):

[10.1029/2021JB022244](https://doi.org/10.1029/2021JB022244)

Link:

[Link to publication record in Edinburgh Research Explorer](#)

Document Version:

Publisher's PDF, also known as Version of record

Published In:

Journal of Geophysical Research. Solid Earth

Publisher Rights Statement:

© 2021. The Authors.

General rights

Copyright for the publications made accessible via the Edinburgh Research Explorer is retained by the author(s) and / or other copyright owners and it is a condition of accessing these publications that users recognise and abide by the legal requirements associated with these rights.

Take down policy

The University of Edinburgh has made every reasonable effort to ensure that Edinburgh Research Explorer content complies with UK legislation. If you believe that the public display of this file breaches copyright please contact openaccess@ed.ac.uk providing details, and we will remove access to the work immediately and investigate your claim.







Uplift and Seismicity Driven by Magmatic Inflation at Sierra Negra Volcano, Galápagos Islands



Key Points:

- Seismicity and deformation rates varied systematically over 15 years before and after the 2018 eruption of Sierra Negra volcano
- Seismicity rates increase exponentially with total uplift as stress increases on an intracaldera fault system
- Joint analysis of seismicity and deformation is key for understanding evolution of edifice prior to eruption

Andrew Forbes Bell¹ , Stephen Hernandez² , Peter Christopher La Femina³ , and Mario Calixto Ruiz² 

¹School of GeoSciences, University of Edinburgh, Edinburgh, UK, ²Instituto Geofísico, Escuela Politécnica Nacional, Quito, Ecuador, ³Department of Geosciences, The Pennsylvania State University, University Park, PA, USA

Correspondence to:

A. F. Bell,
a.bell@ed.ac.uk

Citation:

Bell, A. F., Hernandez, S., La Femina, P. C., & Ruiz, M. C. (2021). Uplift and seismicity driven by magmatic inflation at Sierra Negra volcano, Galápagos Islands. *Journal of Geophysical Research: Solid Earth*, 126, e2021JB022244. <https://doi.org/10.1029/2021JB022244>

Received 15 APR 2021
Accepted 26 JUN 2021

Abstract Although episodes of surface uplift and elevated seismicity precede many volcanic eruptions, their temporal evolution is often complex, and apparently in contradiction to simple trends predicted by mechanical deformation models. Here, we use continuous global positioning system and seismic data recorded at Sierra Negra volcano, Galápagos Islands, to show how the edifice responded to stress changes driven by magma accumulation in a shallow sill. The rate of uplift varied during the 13 years and 6.5 m of inflation before the 2018 eruption. The number of earthquakes per unit of uplift increased exponentially with total uplift as the differential stress increased. Accordingly, the temporal seismicity rate varied in time as a function of both the total uplift and the uplift rate. The Gutenberg-Richter b -value decreased as a function of total uplift. In the final six months before the eruption, a sequence of large ($M > 4$) earthquakes regulated the state of stress on the fault, each being followed by 2–3 days of postseismic quiescence, and retarding the increase in seismicity rate. These earthquakes did not affect the overall uplift rate. Subsidence of 8.5 m accompanied the 2-month eruption. On resumption of uplift, the number of earthquakes per unit of uplift was very low, and the b -value high, reflecting the relaxed stress state of the fault system. These observations show that crustal deformation becomes increasingly brittle at higher stress states, and supports theoretical models based on elastic-brittle mechanics. They suggest that joint interpretation of deformation and seismicity is key for forecasting future eruptions in similar volcanic settings.

Plain Language Summary The accumulation and withdrawal of magma within a volcano changes the stress in the surrounding rocks. These stress changes in turn can cause deformation of the volcano's surface, and earthquakes in the edifice—signals that are possible to detect and quantify using GPS and seismometers. Understanding the nature and relation between surface deformation and seismicity may provide a key to improved forecasting of volcanic activity, but high-quality observations through prolonged episodes of magma accumulation are rare. Here, we describe ground deformation and seismicity data recorded at Sierra Negra volcano, Galápagos Islands, before and after the 2018 eruption. We observe a systematic increase in the earthquake rate with both total uplift and uplift rate as stress progressively increased in the edifice. These trends were accompanied by changes in the proportions of large and small earthquakes, and are consistent with theoretical models of rock deformation. Our results support the value in joint analysis of deformation and seismicity data for tracking and forecasting the evolution of volcanic unrest.

1. Introduction

Volcanic eruptions are often preceded by surface uplift and elevated seismicity (Amelung et al., 2000; Biggs et al., 2010; Chadwick et al., 2006; Nooner & Chadwick, 2016; Robertson & Kilburn, 2016). Such signals can be the first indication of an approaching eruption, and their spatial and temporal patterns form the basis for short-term eruption forecasts (Sparks, 2003; Voight, 1988; White & McCausland, 2019). A simplified, reductionist, paradigm for the approach to volcanic eruption involves the progressive pressurization of a shallow magma reservoir until the excess pressure exceeds the tensile strength of the reservoir margins. At this point, the reservoir fails, and magma can ascend to the surface (Gudmundsson, 2012). Before reservoir failure occurs, the volcanic edifice deforms in response to the increased pressure, commonly resulting in surface uplift, and high-frequency volcano-tectonic (VT) seismicity where the differential stress exceeds the local brittle failure criteria. Consequently, in circumstances where this model is valid, spatio-temporal

© 2021. The Authors.

This is an open access article under the terms of the [Creative Commons Attribution License](https://creativecommons.org/licenses/by/4.0/), which permits use, distribution and reproduction in any medium, provided the original work is properly cited.

patterns of uplift and seismicity reflect the evolution of stress conditions and local proximity to material failure within the edifice (Roman & Cashman, 2006), and may allow us to identify, or even forecast, the timing of reservoir failure.

Voight (1988) proposed an empirical relation to describe the evolution of rates of geophysical and geodetic parameters with time before volcanic eruptions, where the acceleration in a parameter Ω (such as uplift or number of earthquakes) is related to its rate by

$$\frac{d^2\Omega}{dt^2} = K \left(\frac{d\Omega}{dt} \right)^\alpha, \quad (1)$$

where α and K are constants. Solutions to Equation 1 involve an exponential acceleration of parameter rate with time in the case that $\alpha = 1$, and an inverse power-law acceleration in time in the case that $\alpha > 1$. The power-law exponent is given by $p = 1 / (1 - \alpha)$, so the acceleration is hyperbolic if $\alpha = 2$. Relations of the form of Equation 1 emerge from the statistical properties of systems approaching a critical state (Rundle et al., 2003). In the case of precursors to volcanic eruptions, Equation 1 is commonly interpreted in terms of the physics of material failure (Voight, 1989), with fracture growth and interaction within the edifice in response to elevated magma pressure leading to the onset of eruption as the realization of a through-going failure of the edifice (Kilburn, 2003; Kilburn & Voight, 1998).

Many volcanic eruptions are apparently not preceded by clear systematic trends in seismicity or deformation. A continuum of preeruptive states exist, from fully open systems where magma and gas are free to flow to the surface, through partly and variously plugged systems, to entirely closed systems, reawakening after long periods in repose. Even at closed volcanic systems, reservoir failure can be achieved through a variety of mechanisms that may not involve extended episodes of deformation. Failure may result from rapid changes in stress in the edifice, for example, induced by flank slip or large regional earthquakes. The ascent of highly over-pressured magma from depth or rapid vesiculation may suddenly increase the magma pressure in the shallow reservoir, leading to rapid failure. However, even at eruptions preceded by prolonged episodes of surface uplift and seismicity, apparently driven by pressurization of a shallow reservoir, observed precursory trends often do not follow Equation 1. This is particularly apparent at caldera volcanoes, where years or decades of preeruptive inflation are associated with very variable rates of uplift and seismicity (Kilburn et al., 2017; Robertson & Kilburn, 2016).

Kilburn et al. (2017) and Kilburn (2018) argue that some of the discrepancies between observed precursory trends and Equation 1 might be explained by the complex stress evolution during extended inflationary episodes, and the different behaviors of edifice strain and seismicity. Using a model based on elastic-brittle rheology and statistical mechanics, they suggest that during a primary “quasi-elastic” regime of deformation, as differential stress increases due to pressurization of the magma chamber, strain is largely elastic. Differential stress should increase linearly with measures of bulk strain (such as total uplift), but the number of earthquakes per unit of uplift should increase exponentially as faults become progressively stressed. Once the differential stress reaches a critical threshold, termed the “characteristic stress,” deformation enters the inelastic regime, and both seismicity and strain should increase hyperbolically with differential stress, until the edifice fails. In this regime, no further strain can be accommodated elastically, and all new strain is entirely accommodated by movement on faults. In some instances, a period of steady inelastic seismicity and strain rates may precede the transition to the hyperbolic regime (Kilburn, 2018).

Accordingly, understanding how the differential stress increases with time is key to interpreting trends in uplift and seismicity rates. In the quasi-elastic regime, the linear relation between differential stress and strain means that the number of earthquakes per unit of uplift should increase exponentially with total uplift. The evolution of seismicity rates with time depends on the details of the stressing rate, which is likely to be controlled, at least in part, by the supply of magma from depth. Voight’s relation (Equation 1) holds in the special case that stressing rate is constant.

There are few high-quality observations of surface deformation and seismicity through full inflationary episodes and eruptions. The events themselves are rare and require long-term maintenance of ground-based monitoring networks. Consequently, there are few data sets with which to investigate the details of temporal changes in deformation and seismicity, or to test different models. Here, we describe the surface

deformation and seismicity recorded between 2005 and 2019 at Sierra Negra, a basaltic caldera volcano on Isabela Island, Galápagos Islands (Bell et al., 2021). Sierra Negra presents a rare opportunity to investigate the evolution of seismicity in a single deforming system, and a single fault system, across a wide range of stress states. Through 13 years of inflation before the 2018 eruption, uplift and seismicity rates vary with time, but the number of earthquakes per unit of uplift increases exponentially with total uplift. Seismicity rates, therefore, depend on both the total uplift and the uplift rate. The Gutenberg-Richter b -value decreased linearly with total uplift. In the final 6 months of inflation before the eruption seismicity rates no longer increased with total uplift. A sequence of large ($M > 4$) earthquakes during this time were followed by 2–3 days of seismic quiescence, indicating a transient drop in stress levels on the seismogenic fault systems. After the end of the 2-month eruption, high reinflation rates were accompanied by low seismicity rates and a high seismic b -value, consistent with a drop in overall stress conditions.

First, we describe the overall trends in seismicity and ground deformation at Sierra Negra before and after the 2018 eruption. We then analyze the rates of seismicity associated with large system-scale faulting events. Finally, we discuss implications of these observations for volcanic and magmatic processes, and eruption forecasts.

2. Background—Sierra Negra and the Inflation-Deflation Cycle of the 2018 Eruption

The basaltic shield volcanoes of the Galápagos Islands, Ecuador, are amongst the most active volcanoes on Earth. The seven volcanoes of the western islands of Isabela and Fernandina (Figure 1a) have a distinct morphology defined by relatively steep upper flanks and well-developed calderas (Harpp & Geist, 2018; Poland, 2014). Amongst these, there is considerable variation from the deep, narrow calderas of Fernandina and Cerro Azul in the west, and the wide, shallow calderas of Alcedo and Sierra Negra in the east (Cullen et al., 1987). Growing topography is associated with prominent intracaldera fault systems at Alcedo and Sierra Negra, and suggest that these calderas are currently undergoing resurgence (Amelung et al., 2000; Bell et al., 2021; Galetto et al., 2019; Jónsson, 2009).

The remote location of the islands means that ground-based geophysical and geodetic monitoring is logistically challenging. Regional and teleseismic recordings indicate that many historical eruptions at Galápagos volcanoes are associated with earthquakes of $M4$ and greater (Chadwick et al., 2006; Filson et al., 1973; Geist et al., 2008; Simkin & Howard, 1970; Squires, 1979). Evidence for coastal uplift also indicates that these have been the site of many meters of ground deformation (Poland, 2014). More recently, InSAR observations have confirmed that all of the western Galápagos volcanoes undergo significant amounts of ground deformation (Bagnardi & Amelung, 2012; Galetto et al., 2019; Jónsson et al., 2005).

Sierra Negra volcano is located in the south of Isabela Island (Figure 1a). The edifice is 40 km across, reaches a maximum elevation of 1,100 m, and contains a 120 m deep caldera that is, 7 by 9 km across (Figure 1b). Within the caldera, a C-shaped fault system (Figure 1b) is known to be the source of $>M4$ earthquakes in the approach to and onset of eruptions (Bell et al., 2021; Chadwick et al., 2006; Geist et al., 2008). The fault system is consistent with a trapdoor caldera morphology (Acocella, 2007), accommodating preeruptive uplift of the inner caldera during inflation, and subsidence during coeruptive deflation (Bell et al., 2021; Jónsson, 2009). Net uplift since the caldera-forming event has resulted in permanent uplift (resurgence) of the inner caldera, such that the trapdoor fault ridge rises above the caldera rim.

The recent eruptive history of Sierra Negra includes eruptions in 1979, 2005, and 2018. The 1979 eruption (Squires, 1979) occurred before the installation of geodetic or seismic monitoring equipment on Isabela island. The 2005 eruption of Sierra Negra was observed by a local cGPS network and InSAR (Amelung et al., 2000; Chadwick et al., 2006; Jónsson et al., 2005). These data reveal large preeruptive inflation and rapid coeruptive subsidence (Figure 2a), although the total uplift is not known. There were no seismometers located on Isabela during the 2005 eruption; however, preeruptive seismicity occurred in the lead up to the eruption and was located on the trapdoor fault system (Chadwick et al., 2006).

On June 26, 2018, a basaltic fissure eruption began on the northern rim of the caldera, with fissure systems rapidly opening on the northern and northwestern flanks (Bell et al., 2021; Vasconez et al., 2018). The

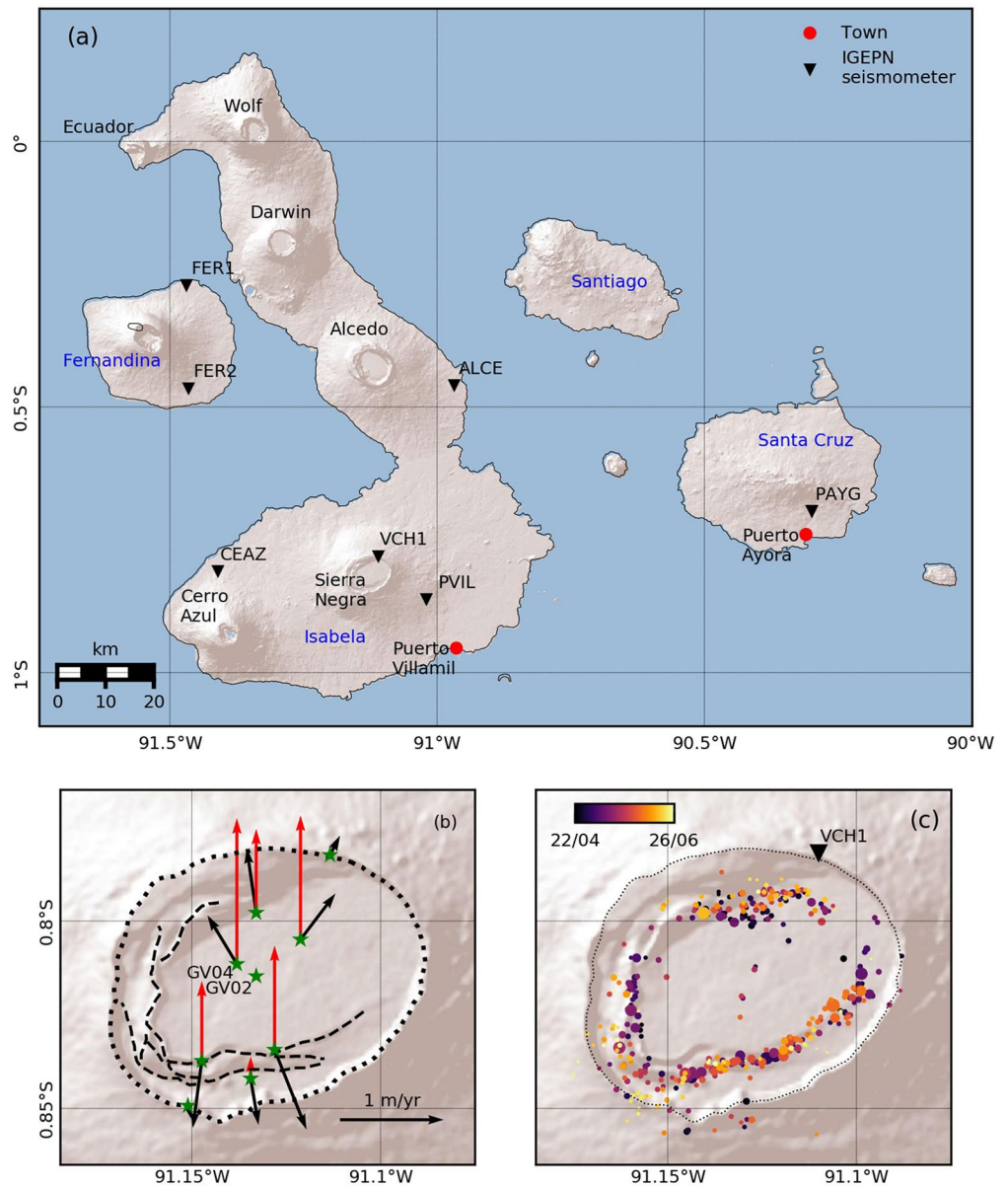


Figure 1. Maps of Sierra Negra volcano, key structural features, deformation, and seismicity. (a) The western islands of the Galápagos archipelago, showing locations of caldera volcanoes of the islands of Isabela and Fernandina, the permanent seismic monitoring network of the Instituto Geofísico, Escuela Politécnica Nacional, and the towns of Puerto Villamil and Puerto Ayora. (b) Average surface uplift (red arrows) and horizontal displacement (black arrows) rates recorded by the continuous global positioning system network between January 01 and June 26, 2018. Location of C-shaped trapdoor fault system indicated by black dashed lines, and caldera rim by black dotted line. Approximate area of trapdoor indicated by gray shading, and location of trapdoor “hinge” indicated by white squares. (c) Epicenters of earthquakes located by the IGUANA network, April 24–June 26, 2018, colored by time of occurrence.

eruption continued until August 25, 2018, producing lava flows which covered an area of 31 km² and a volume of 0.14 ± 0.07 km³ DRE. The eruption was preceded by >6.5 m uplift in the center of the caldera, driven by inflation of a shallow magma chamber at a depth of 2 km. Uplift was accompanied by high rates of seismicity, many with magnitudes above M13.0, and including an event with Mw5.4 a few hours before the onset of the eruption. During the eruption, the caldera subsided by 8.5 m. Subsidence was initially extremely rapid, and gradually slowed over the 2-month eruption.

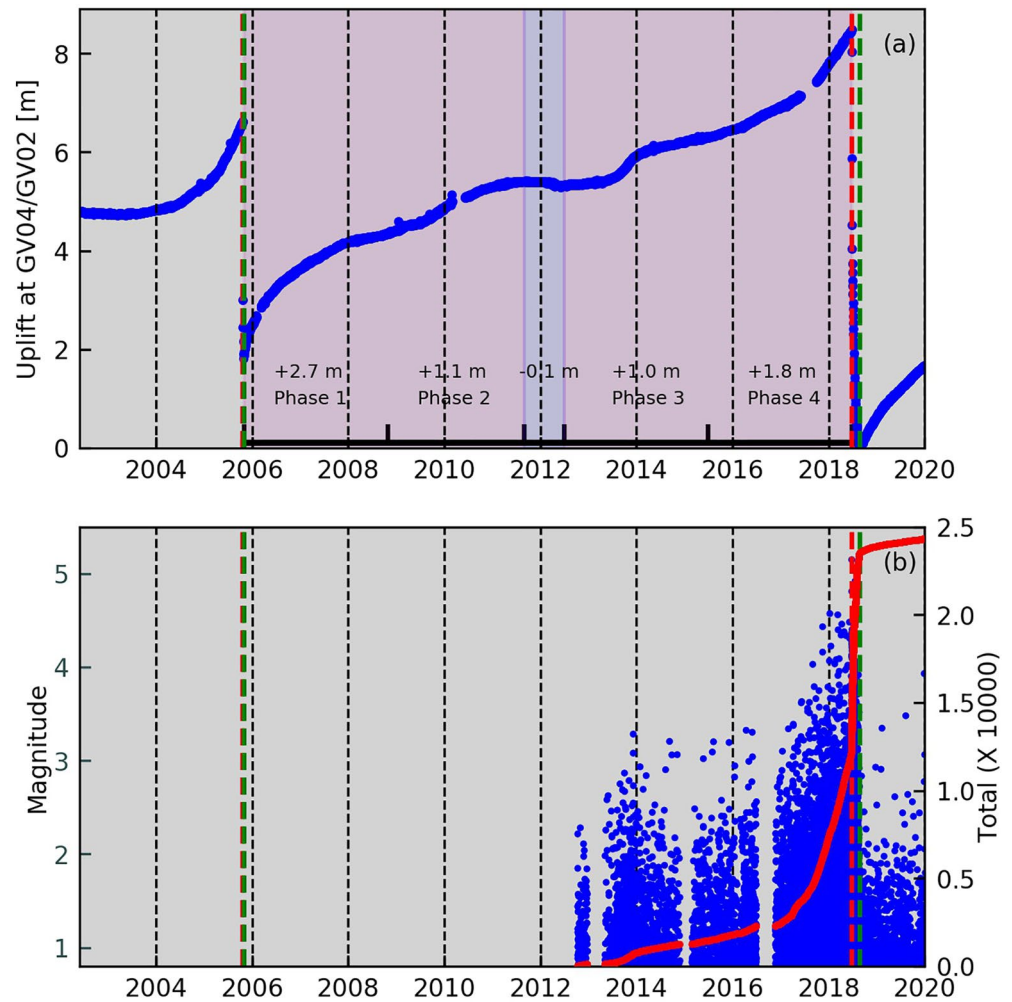


Figure 2. Surface deformation and seismicity recorded at Sierra Negra (a) Uplift recorded by continuous global positioning system stations GV02 and GV04 in the center of the caldera between 2002 and 2020. Red and green dashed lines indicate time of eruption onset and end, respectively. Phases of uplift (light red) and subsidence (light blue) indicated by shading. (b) Magnitudes (blue points) and total $M > 0.8$ earthquakes (red line) from the installation of station VCH1 in 2012 until 2020.

3. Data

The 2018 eruption at Sierra Negra was the first eruption on the Galápagos Islands to be recorded by a local multiparametric monitoring network. This study focuses on the time series of cGPS and seismic data.

3.1. cGPS data

The Continuous Global Positioning System (cGPS) network on Sierra Negra was initiated in 2002 with a mix of two dual-frequency and eight single frequency receivers. The network was then upgraded in 2010 to all dual-frequency receivers, collecting data every 30 s, and later following the 2018 eruption to record at 5 Hz, 1 Hz, and 30 s. The network continues to run at the time of this writing. The data were processed for daily static positions and high-rate (1 epoch/30 s) kinematic positions using the precise point positioning (PPP) method implemented in the GIPSY-OASIS II version 6.3 software (Zumberge et al., 1997). For the daily static positions, phase ambiguity resolution was performed using the single receiver algorithm (Bertiger et al., 2010), and we used final satellite ephemerides provided by the Jet Propulsion Laboratory. Final daily solutions were transformed into the IGB08 reference frame (Reibischung et al., 2012). Kinematic analysis followed (Larson & Miyazaki, 2008), where we applied ocean loading corrections using FES2004 (Lyard

et al., 2006), and modeled wet and dry tropospheric zenith delays with VMF1 mapping functions (Boehm et al., 2006). The cGPS 30 s data were used to produce kinematic time series to investigate coseismic displacements for preruptive and syneruptive earthquakes and deformation within the Sierra Negra caldera related to magma migration.

The spatial distribution of displacements recorded on the cGPS network during uplift (Figure 1b) is consistent with elastic deformation driven by inflation of a flat-topped magma body (Yun et al., 2006), most likely a sill, located at a depth of 2 km below the caldera surface. Coseismic displacements associated with preruptive and coeruptive $M > 4.0$ earthquakes on the trapdoor fault system are superimposed on this pattern. The amplitude of uplift is greatest at stations GV02 and GV04 in the center of caldera (Figure 1b), consistent with InSAR time series, and decreases to the edge of the trapdoor fault system. The time series of uplift at GV02/GV04 thus provides the most appropriate measure of caldera uplift, and demonstrates four phases of preruptive inflation and one phase of preruptive subsidence (Figure 2a).

3.2. Seismic Data

Seismic stations in the permanent network of the Instituto Geofísico, Escuela Politécnica Nacional (IGE-PN) were first installed in the Galápagos in late 2012 (Alvarado et al., 2018). The sparse six station network means that only large earthquakes are detected on multiple stations, and so the completeness magnitude and location uncertainties are high. However, the Trillium compact 120 three-component broadband seismometer “VCH1” is located on the NE rim of Sierra Negra caldera (Figure 1c), and provides an excellent record of seismicity at Sierra Negra, though with the limitations imposed by single-station detections. The station has been largely operational since October 2012, though with some occasional data gaps. Station GS09 of the SIGNET deployment, operational between late 2009 and 2011 (Tepp et al., 2014), was installed at a site close to that later occupied by VCH1. The lack of overlap between the SIGNET and IGE-PN networks means that a direct comparison between the two data sets using the methods employed in this study is difficult.

In Late April 2018, the 14-instrument IGUANA seismic network was installed at Sierra Negra, and remains operational at the time of writing (Bell et al., 2021). Data collected using this network were processed in order to construct a high-precision catalog of earthquake locations in the final stages of inflation before the 2018 eruption, coeruptive deflation, and posteruptive reinflation. Almost all earthquakes were located on the intracaldera trapdoor fault system (Figure 1c), at shallow depths, above the top of the sill at 2-km depth.

4. Methods

4.1. Earthquake Occurrence Times

Data from station VCH1 are used to determine the time series of earthquakes at Sierra Negra. To detect local events, data are band pass filtered between 5 and 10 Hz, and an STA/LTA algorithm is implemented in ObsPy (Krischer et al., 2015). A trigger is required on all three components of the single-station data, and triggers with anomalous frequency content, very short trigger durations, or very short interevent times are removed. The high reliability of the algorithm is verified by inspection of hundreds of events. We argue that almost all small high frequency earthquakes detected in this way are located at Sierra Negra, apart from known short-lived seismic episodes associated with eruptions at Fernandina in 2017 and 2018, and an intrusion at Cerro Azul volcano in 2017.

4.2. Earthquake Magnitudes

For each detected earthquake, we determine the root mean square amplitude of the vertical component of the velocity in a 10-s window around the peak amplitude, in a 1–20 Hz frequency band. Local earthquake magnitudes are then assigned based on a linear calibration of the logarithm of the root mean squared amplitude at VCH1 and the magnitude of located events coreported in the IGUANA catalog from April 2018. We correct for source distance from VCH1 using a correlation between distance and rate of coda amplitude decay. We argue that this method is appropriate because earthquakes during inflation at Sierra Negra are almost entirely located on the shallow trapdoor fault. Seismicity rates estimated in this way broadly follow

those based on the less-complete IGEPN catalog of located events. The frequency content and s-p times of automatically detected events are similar to those recorded during the IGUANA deployment, suggesting that earthquake locations do not change systematically in time. Magnitudes estimated by this method assume events are equidistant from VCH1, a reasonable approximation for events located on the southern and western TDF, but likely overestimates the magnitudes of events on the northern TDF by ~ 0.5 units. We treat each earthquake magnitude (M) as a moment magnitude, and estimate the seismic moment (M_0 ; in Nm) associated with each using the scaling relation (Kanamori, 1977; Pancha et al., 2006)

$$M_0 = 10^{1.5M+9.095} \quad (2)$$

The seismic moment, M_0 , is an indirect measure of the energy released during an earthquake and is defined as

$$M_0 = \mu AD \quad (3)$$

where μ is the shear modulus of the rock, A is the area of rupture on the fault, and D is the average slip (Kanamori, 1977). We sum the seismic moment released by each earthquake to provide an estimate of the energy released by earthquakes through time, and as a comparison to the total energy associated with edifice displacements (see Section 4.5).

4.3. Earthquake Catalog Quality

When basing an analysis on rates and magnitudes of earthquakes reported in a catalog, it is important to ensure that artifacts and spurious results are not introduced by changes in the completeness of the catalog. As we use earthquake detections and amplitudes from a single station, installed for the duration of our study, there is limited scope for these issues to arise. Their potential impact is also dependent on the nature of the analysis being undertaken. For example, a small underestimation of the magnitude of completeness can lead to large errors in the estimation of the Gutenberg-Richter b -value.

The most likely source of variable catalog completeness over longer time scales is due to underdetection of small amplitude events at times of higher earthquake rates. This effect would result in relative underestimation of high earthquake rates, and is certainly apparent during the extremely high earthquake rates accompanying coeruptive deflation. Over shorter times scales, diurnal noise variations (at Sierra Negra due to increased wind, thermal noise, and tourist visitors during the day), and seasonal storms and ocean noise (VCH1 is 30 km from the ocean), may lead to variations in catalog completeness.

The standard approach to deal with potential changes in the reporting of earthquake magnitudes is to apply a minimum magnitude threshold to the catalog before undertaking further analyses. Ideally, this threshold corresponds to the “completeness magnitude” of the catalog—the smallest magnitude above which all earthquakes occur in the spatial-temporal area of interest are recorded in the catalog. We employ several different methods to investigate consistency of reporting in our catalog and determine a minimum magnitude threshold. We compare day and night time earthquake rates as a function of time, and estimate the completeness magnitude using a variety of standard methods (Roberts et al., 2015) based on the assumption that the magnitude distribution follows the Gutenberg-Richter relation. As described in Section 5.2, this assumption may not be valid. Importantly, we test all our analyses using a variety of minimum magnitude thresholds, and ensure that our key results do not depend on this choice. For most of our analysis, our preferred minimum magnitude threshold is $M_{0.8}$, based on analysis of the b -value stability function at the highest preeruption earthquake rates. This approach assumes that the location of earthquakes is stationary over time (not moving systematically closer to or further from VCH1).

4.4. Statistical Methods

We determine the Gutenberg-Richter b -value of the earthquake frequency-magnitude distribution (Gutenberg & Richter, 1954) using the maximum-likelihood method (Aki, 1965; Roberts et al., 2015). We analyze the evolution of the b -value through time, using consecutive samples of 1,000 events greater than minimum magnitude threshold (hence associated with variably sized time windows). In tectonic settings, the b -value

is typically around 1.0, with lower values commonly believed to reflect high differential stresses (Schorlemmer et al., 2005). In volcanic settings, b -values are more variable, though systematic patterns and trends are elusive (Roberts et al., 2015).

In Section 5.2, we discuss the stability of this value as a function of minimum magnitude threshold. In Section 5.1, we model the change in seismicity rate dn / dz with total uplift, z , using the model of Kilburn (2018), estimating posterior distributions of the amplitude, k , and rate, λ , parameters of an exponential relation:

$$\frac{dn}{dz} = ke^{\lambda z} \quad (4)$$

We apply this model using the Bayesian Point Process method described by Bell (2018) and Bell et al. (2018). We use half Normal distributions as prior distributions for model parameters k and λ , though the inversion is insensitive to this choice. We run 10,000 Markov Chain Monte Carlo iterations, implemented with PyMC3 (Salvatier et al., 2016). To complete this model, we interpolate the small temporal seismic data gaps with a synthetic earthquake time series generated according to the optimal exponential rate model. This is an iterative process, estimating an initial model using the incomplete data, and repeating until the solution converges (in three or four iterations).

4.5. Geodetic Moment

The geodetic moment provides a measure of the energy involved in total deformation of the volcanic edifice, and a comparison to the energy released by earthquakes. A comparison of the seismic and geodetic moment rates provides insights into the nature of the deformation process, and an indication of how brittle the system is (Pancha et al., 2006). cGPS data indicate that the relative spatial distribution of uplift does not change with time. Consequently, we estimate the geodetic moment of deformation through time at Sierra Negra as a linear function of the maximum uplift rate. Using a modified form of the expression of Anderson (1979), the geodetic moment rate is given by

$$\dot{M}_0 = 2\mu\Sigma W\dot{\epsilon} \quad (5)$$

where $\mu = 3 \times 10^{10} \text{ Nm}^{-2}$ is the shear modulus, $\Sigma = \pi r^2$ is the surface area of the region, W is the thickness of the deforming region, and $\dot{\epsilon} = V / r$ is the strain rate (Pancha et al., 2006), where V is the maximum uplift rate. We approximate the deforming caldera as a circular region, with radius $r = 4000$ m and thickness $W = 2000$ m, equivalent of the depth to the sill. The maximum uplift rate V , and hence strain rate, through time can be calculated using the uplift at cGPS stations GV04 and GV02, located close to the location of maximum uplift (Bell et al., 2021). For every meter of uplift at GV04, we use the spatial distribution of uplift from InSAR to estimate the maximum uplift at the center of the caldera is 1.14 m. This calculation indicates that for every meter of uplift, the moment is $1.5 \times 10^{18} \text{ Nm}$. Using Equation 2, this moment is equivalent to that expected for a moment magnitude Mw6.1 earthquake, much larger than any earthquake recorded during the unrest. Consequently, only a small fraction of total geodetic energy is associated with brittle faulting.

5. Results

5.1. Seismicity and Uplift Rates

Uplift began immediately after the end of both the 2005 and 2018 eruptions (Figure 2a). This rapid return to uplift suggests continued connectivity between the shallow sill and a deeper magma storage region. Initial high post-eruptive uplift rates slowed with time, consistent with an equilibration of pressure between the two reservoirs. Between the end of the 2005 eruption and the start of the 2018 eruption the uplift rate varied in time.

Over time scales of weeks to months, changes in seismicity rate broadly follow changes in uplift rate (Figure 3). Seismic moment release follows a similar trend to earthquake numbers, though prominent steps are associated with individual large earthquakes. A pulse of increased uplift rate in late 2013 is matched by an increase in earthquake rate (Figure 3a). A further increase in uplift rate in 2017 is also evident in earthquake rates (Figure 3b), as is the decrease in rates following the end of the 2018 eruption and initiation of

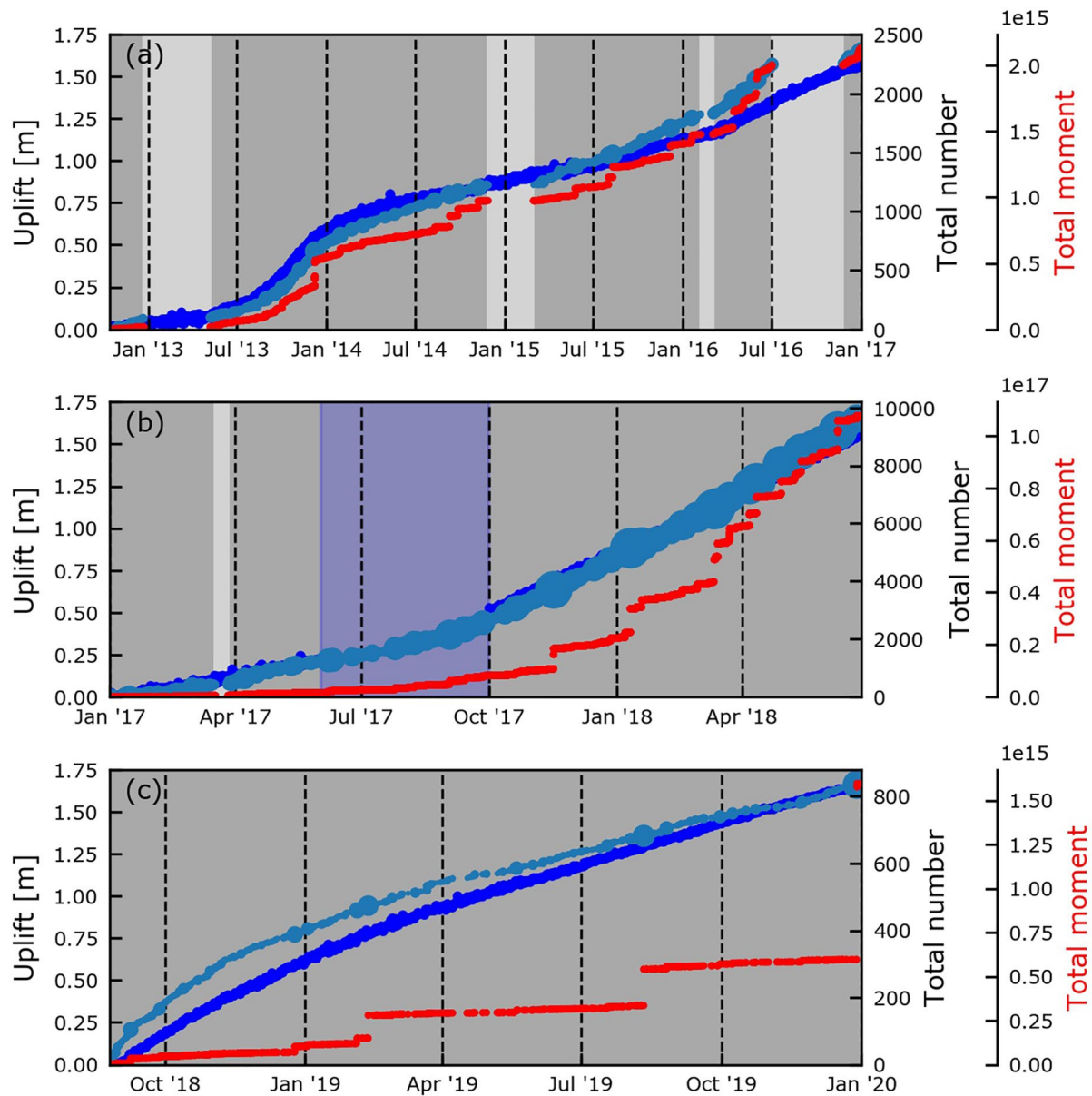


Figure 3. Uplift at GV04 (dark blue), total number of $M \geq 1.2$ earthquakes (light blue), and total seismic moment (red) recorded at Sierra Negra between (a) October 14, 2012 and December 31, 2017, (b) January 01, 2017 and June 26, 2018, and (c) August 26, 2018 and December 31, 2019. Earthquake magnitude indicated by size of light blue circle. Note identical left hand (uplift) y-axis range, but different right-hand (number of earthquakes) y-axis ranges. Seismic data gaps indicated by pale gray bars. Continuous global positioning system data gap indicated by blue bar.

new uplift (Figure 3c). However, there are longer-term changes in earthquake rate. In Figure 3, all three panels have the same left-hand y-axis range (1.75 m uplift), but the right-hand y-axis range for total number of earthquakes is 2,500, 10,000, and 800. This observation suggests that as total uplift increases toward the 2018 eruption, each unit of uplift is associated with a greater number of earthquakes. After the eruption, the uplift rate slows with time. Each unit of uplift is associated with far fewer earthquakes than before the eruption.

The data in Figure 3 suggest that there are variations in the relation between rates of uplift and seismicity with time at Sierra Negra. These relations are shown in Figure 4 as a function of time from the end of the 2005 and 2018 eruptions. Uplift rates (Figure 4b) immediately after the end of the 2005 and 2018 eruptions follow similar decelerating trends with time. Seismicity and uplift rates both increased from 2015 through

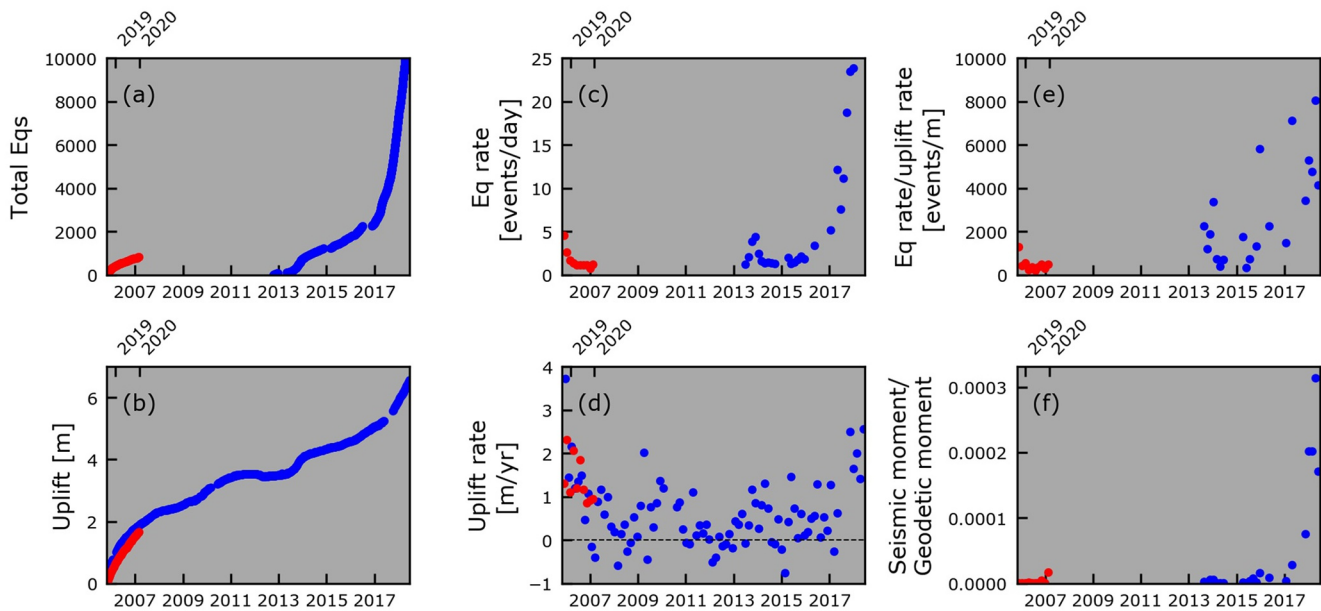


Figure 4. Seismicity and uplift totals (left panels), rates (middle panels), and ratios (right panels) from the end of the 2005 eruption to the start of the 2018 eruption (blue) and from the end of the 2018 eruption (red). Note two sets of x-axes corresponding to post-2005 data (bottom; blue data) and post-2018 data (top; red data).

to late 2017 (Figures 4c and 4d). However, the numbers of earthquakes per unit of uplift also increased, indicating that the seismicity rate increased faster than the uplift rate with time. From late 2017 until the eruption, both seismicity and uplift rates remained high, but did not increase further. The ratio between seismic moment rate and geodetic moment rate increased rapidly toward the eruption (Figure 4f). These observations suggest that as inflation progressed, a larger proportion of the total strain was being released by earthquakes. However, the absolute values are small, reaching a maximum of 0.03% during the preeruptive phase. Therefore, the vast majority of the deformation was accommodated elastically.

The variation in uplift rates through time (Figure 2a) is most likely due to changes in the rate of supply of magma to the shallow reservoir and consequent pressurization (Bell et al., 2021). It is evident that the seismicity rate varies to some extent with uplift rate, but it also broadly increases toward the eruption—though not as a simple function of time predicted by Equation 1. However, a more systematic trend is apparent in the evolution of seismicity as a function of total uplift (Figure 5). The number of earthquakes per unit of uplift during the early stages of inflation after the 2018 eruption is low and apparently constant (Figures 5a and 5b). Likewise, the seismic moment rate is low (Figures 5c and 5d). By the time that consistent seismic monitoring began after the 2005 eruption in late 2012, the center of the caldera had risen by 3.5 m. At that point, the number of earthquakes per unit of uplift was double that observed after the 2018 eruption. The earthquake rate (and hence total number of earthquakes) per unit uplift then increased exponentially until ~5.8 m of total uplift (in late 2017). The exponential rate constant, λ , of the acceleration is 0.88 (Equation 4). At this point, the number of earthquakes per unit of uplift remained constant until the onset of the eruption. The seismic moment release per unit of uplift continued to increase, however.

5.2. Earthquake Frequency-Magnitude Distributions

The b -value changes with uplift alongside changes in earthquake rate (Figure 5e), reflecting a change in the relative rates of earthquakes of different magnitudes as inflation progresses. At the time that consistent seismic monitoring began after the 2005 eruption in late 2012 the b -value was 0.84. It then decreased, apparently as an approximately linear function of total uplift, until it reached 0.7 at the start of the eruption. During the early stages of inflation after the 2018 eruption, the b -value is 1.1.

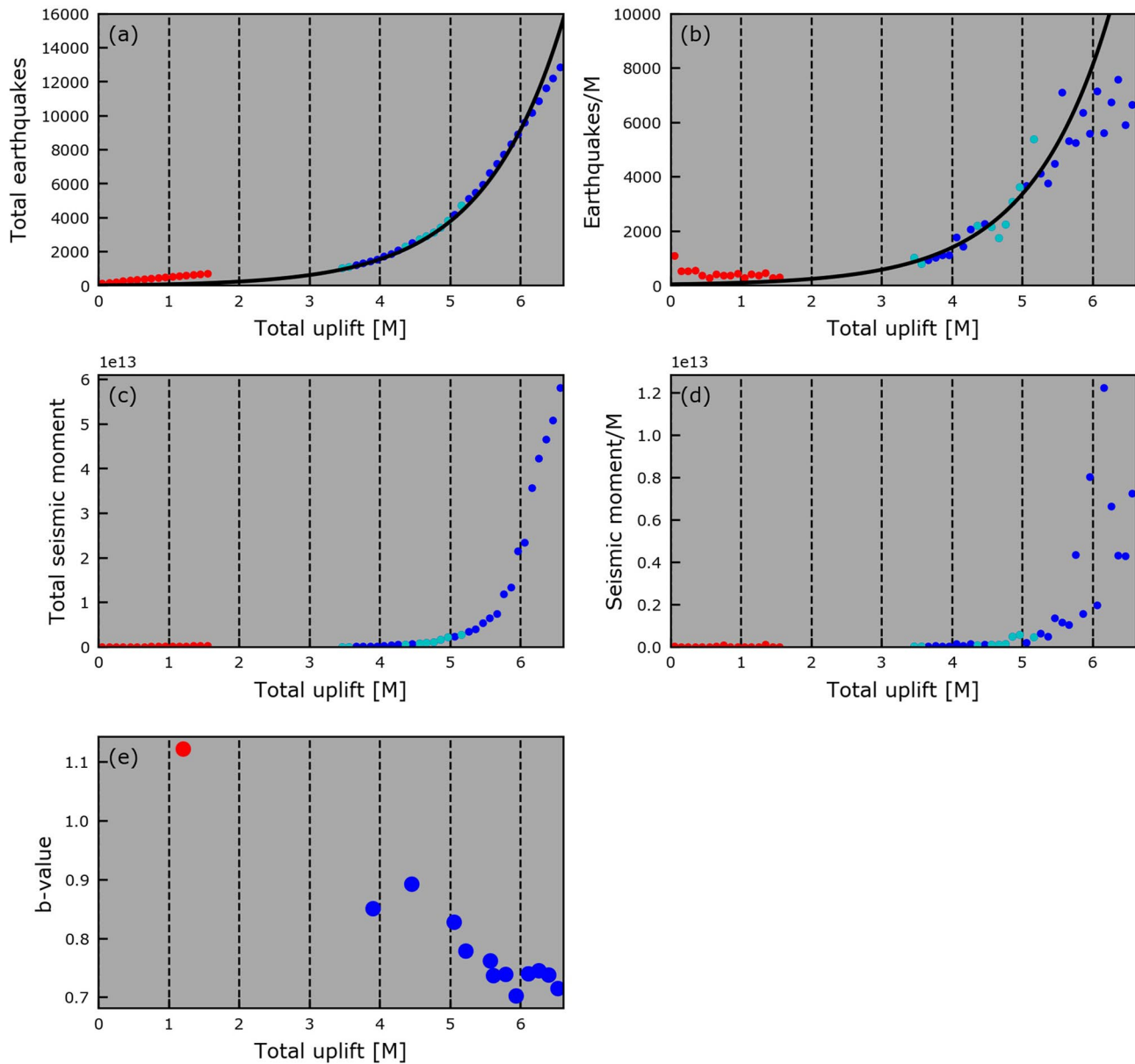


Figure 5. Seismicity as a function of total uplift from the end of the 2005 eruption to the start of the 2018 eruption (blue) and from the end of the 2018 eruption (red). (a) Total number of earthquakes. Black line indicates best exponential model (see text). Light blue points indicate data gaps filled with best exponential model, and total number of earthquakes at start of consistent monitoring at 3.5 m uplift also estimated from exponential model. (b) Earthquake rates per unit of uplift. (c) Total seismic moment release. (d) Seismic moment release rate. (e) Gutenberg-Richter b -value for successive independent successive samples of 1,000 earthquakes.

This change is examined in more detail in Figure 6. An increase in the number of $M > 3$ earthquakes with time is apparent after 2017 (Figure 6a), but this could be explained simply by an increase in earthquake rate. As more earthquakes are recorded in a given time interval at higher earthquake rates, there is a higher chance of recording a rare large event. However, when plotted as a function of event number (Figure 6b), a real increase in the proportion of $M > 3$ and $M > 4$ events is clear before the onset of the 2018 eruption. The high and variable earthquake rates and intermittent tremor during the eruption mean that the completeness magnitude is higher and statistical analysis of seismicity during coeruptive deflation is more challenging, and we omit it here. After the eruption, the proportion of $M > 3$ earthquakes is very low. These changes are evident in the magnitude-frequency distributions of earthquakes through consecutive 1,000 event samples, shown as discrete rates and conventional “Gutenberg-Richter” plots in Figures 6c and 6d. The slope

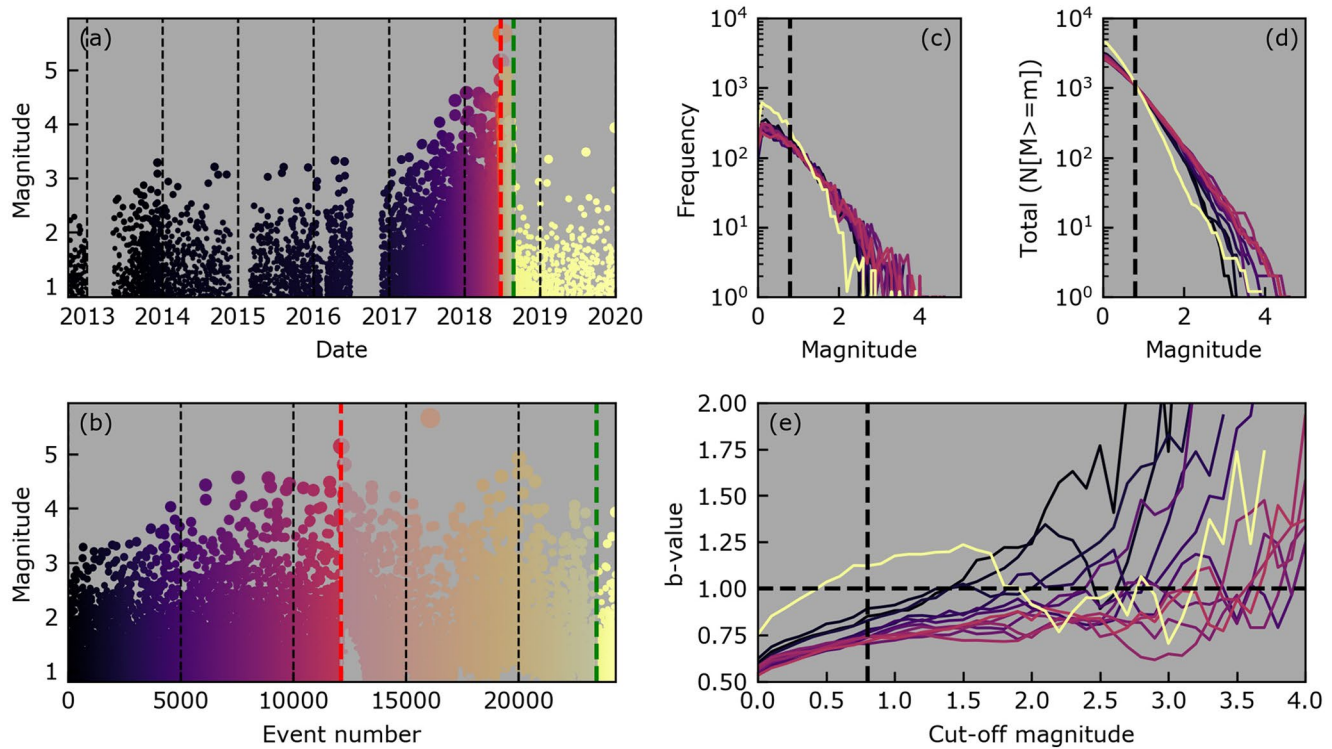


Figure 6. Magnitudes of earthquakes recorded at Sierra Negra 2012–2020. (a) Magnitudes of $M > 0.8$ earthquakes as a function of time. Vertical dashed lines indicate the start (red) and end (green) times of the 2018 eruption. (b) Magnitudes as a function of event number. Colors correspond to those in (a). (c) Discrete and (d) Cumulative magnitude-frequency distributions of consecutive equal size samples of 1,000 $M > 0.8$ earthquakes, colored by time of 500th event (corresponding to colors in (a) and (b)). (e) Stability of the b -value as function of cut-off magnitude for 1,000 event samples in (c) and (d).

of the distribution shallows systematically before the 2018 eruption, reflecting the fall in b -value reported in Figure 5e. The slope of the distribution is steeper after the end of the 2018 eruption. The b -value stability plot (Figure 6e) shows that the temporal trend in b -value is not dependent on the choice of the completeness magnitude, but happens across the full magnitude range. However, the absolute b -values increase with the cut-off magnitude for all preeruptive samples. This pattern is most prominent for early samples, and becomes less marked nearer to the eruption. It suggests that the magnitude-frequency distribution might not follow the simple linear Gutenberg-Richter relation between magnitude and logarithm of frequency. Rather, early distributions are more typical of subcritical frequency size distributions (Main, 1996), approaching a critical condition, with the data more closely approximating a true Gutenberg-Richter distribution, shortly before the eruption.

5.3. Seismic Quiescence Following Large Trapdoor Faulting Earthquakes

From late 2017 through to the start of the eruption in June 2018, the overall uplift and seismicity rates with time at Sierra Negra were approximately constant (Figures 2 and 3). However, during this time a series of notable $M > 4$ earthquakes occurred, some of which were felt by local residents. The uplift rate is not altered by the occurrence of these large earthquakes (Bell et al., 2021). However, inspection of unprocessed seismic data suggested that seismicity rates were elevated before large earthquakes, and suppressed for a few days afterward. Figure 7 shows the seismicity rates for 10 days either side of the 12 largest earthquakes at Sierra Negra between January 01, 2018 and June 25, 2018. For most of these earthquakes, the seismicity rate is higher in the 2–3 days before the earthquake than it is afterward.

This pattern is more evident when aggregated over all the mainshocks (Figure 8). The long-term earthquake rate is stationary through this period, and the aggregate of earthquake rates is not dominated by any one single highly productive sequence. The aggregate rate is above the mean for 2.5 days before the mainshock

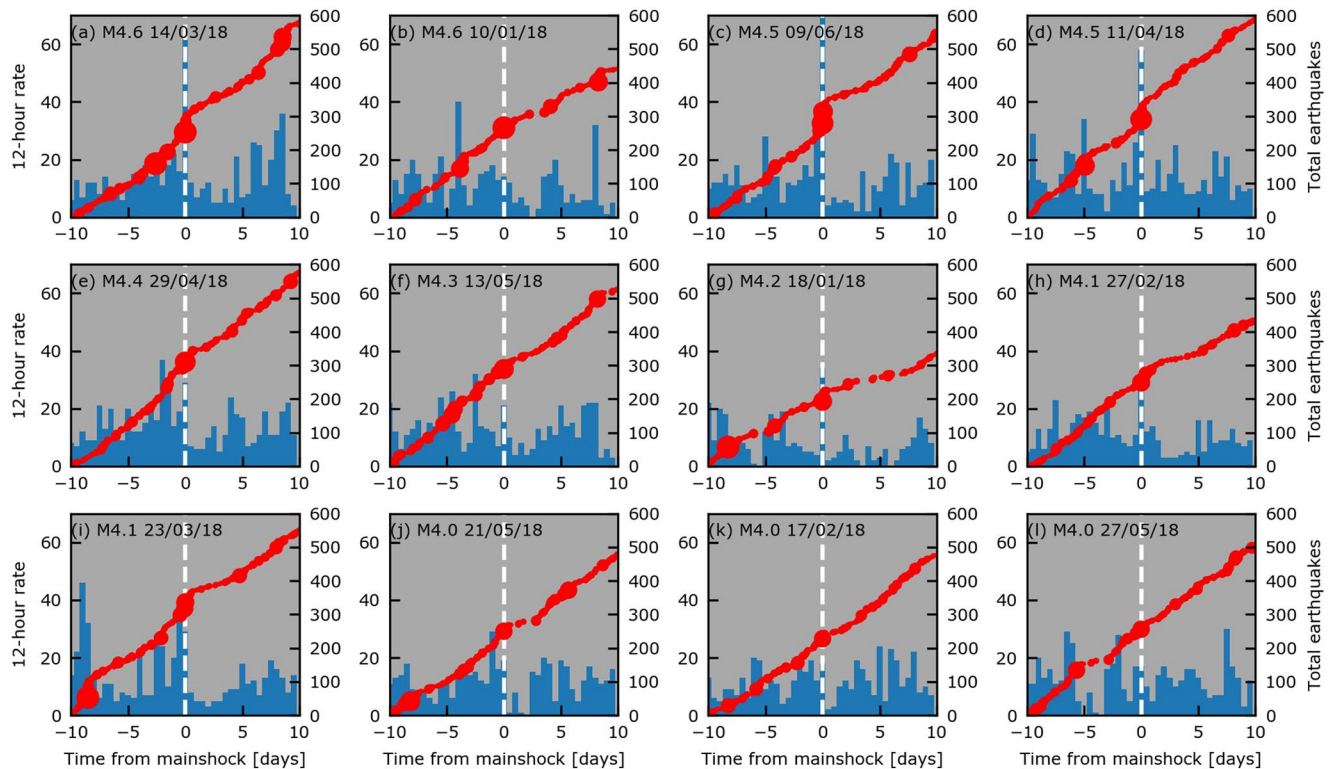


Figure 7. Twelve-hour earthquake rate (blue bars) and total number of earthquakes (red circles) for 10 days before and after 12 of the largest earthquakes recorded at Sierra Negra between January 01, 2018 and June 25, 2018. Circle size is proportional to earthquake magnitude. The “mainshock” earthquakes exclude $M > 4$ earthquakes that occur within 5 days before or after larger events.

time, and lower than the mean for 3 days afterward. Although the mainshocks do trigger immediate aftershocks, the aftershock sequence lasts less than 0.5 days.

6. Discussion

The seismic and cGPS data recorded at Sierra Negra since the end of the 2005 eruption provide new insights into the mechanics of crustal deformation through a cycle of loading and unloading. The overall pattern of deformation during inflation at Sierra Negra is predominantly elastic. Seismicity results from frictional stick-slip on faults within the trapdoor fault system, but the total energy released by this slip contributes a very small amount to the overall geodetic moment. The stress on the TDF is largely relaxed after co-eruptive deflation, but progressively increases as the shallow magma reservoir inflates. Because of this, it presents us with a rare opportunity to investigate the evolution of seismicity in a single fault system across a wide range of stress states.

6.1. Evolution of Seismicity and Uplift Rates

After the end of both the 2005 and 2018 eruptions, uplift rates are high and decrease in a similar manner with time (Figures 2a, 3b and 3d), suggesting that similar processes are acting. These observations are consistent with those from other systems (Björnsson et al., 1979; Tilling & Dvorak, 1993), and physical models based on flow between deep and shallow reservoirs in an elastic medium (Blake & Cortés, 2018), and are likely to be a recurrent feature of deformation following eruptions at Sierra Negra. During inflation before the 2018 eruption, the uplift rate varies with time, including a small subsidence episode. Uplift rates increase through 2017, and remain high but constant during the final 6 months before the eruption. It seems most likely that this temporal variation in uplift rate is controlled by variations in the rate of magma supply to the shallow reservoir, and that this pattern is likely to be unique to each eruption. Inter-eruptive intervals

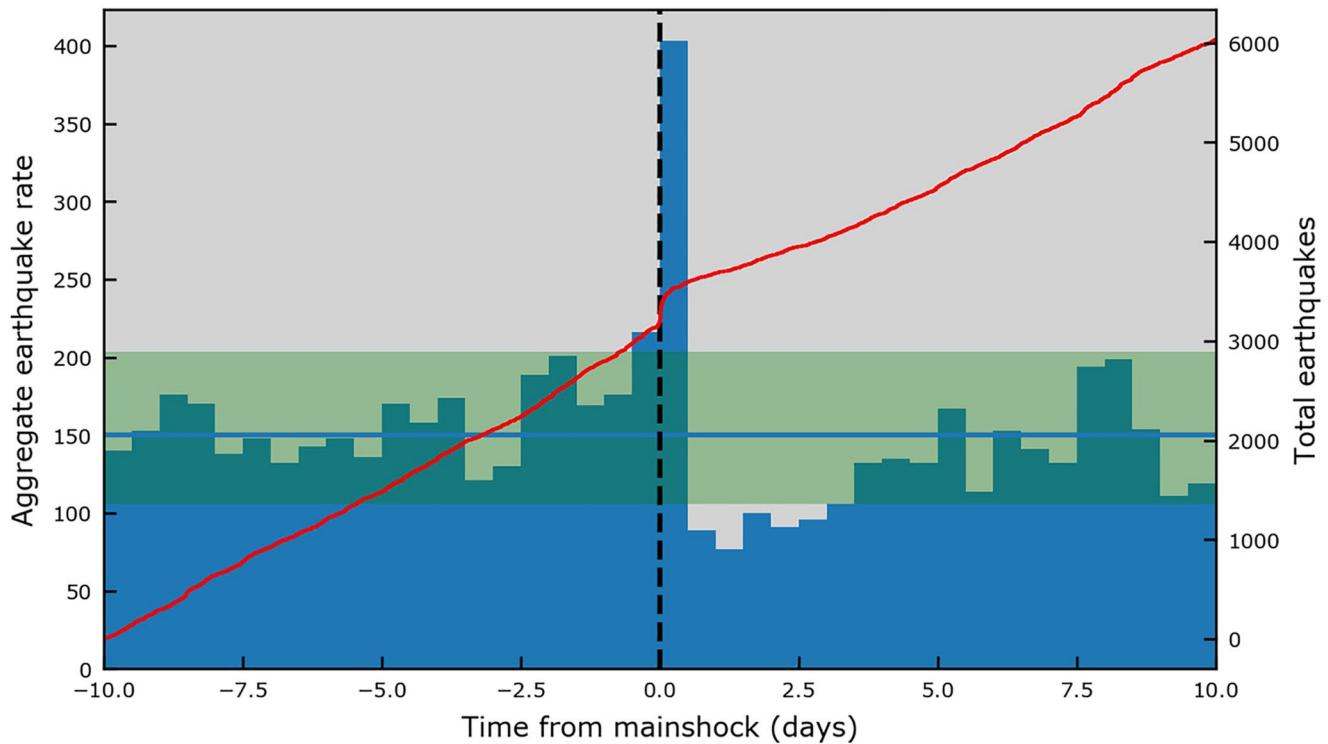


Figure 8. Aggregate half-day earthquake rate (blue bars) and total number of earthquakes (red line) for the 12 mainshocks in Figure 8. Earthquake sequences are superimposed with respect to mainshock occurrence time, indicated by black vertical dashed line. Horizontal blue line and green shading indicate mean and 5% and 95% confidence interval for the half-day rate, bootstrapped from samples January 01 to June 25, 2018.

for recent eruptions at Sierra Negra of 13, 26, 16, and 10 years indeed suggest some variability in magma supply rates. The 2018 eruption began when there had been sufficient total inflation to elevate the stress conditions to a point where the reservoir could fail. The total uplift is an integration of the time-varying uplift rate. However, the coincidence of the eruption onset with a period of high uplift rate is because that happens to be when the stress conditions necessary for eruption triggering were realized.

Variations in the rate of seismicity with time are less systematic than those with total uplift. The rate of seismicity at Sierra Negra during inflation is dependent on both the uplift rate and the total amount of uplift (Figures 3e, 4a and 4b), suggesting that these factors exert the primary control on seismicity rate. Early in the inflationary process, high uplift rates are associated with low seismicity rates. When the total uplift is higher, the same strain rates are associated with much higher seismicity rates. The seismicity rate per unit uplift increases exponentially with total uplift until a total or ~ 5.8 m of uplift, consistent with the “quasi-elastic” phase of the model of Kilburn (2018). These observations indicate that seismicity rates are controlled by the cumulative increase in differential stress on the trapdoor fault system. If, during this phase of deformation, the uplift rate had happened to be constant with time, we suggest that the increase in seismicity rate with time would also have followed an exponential trend, as observed at volcanoes with constant uplift rates (Bell & Kilburn, 2012).

It seems likely that seismicity rates were very low during the initial phase of uplift follow the 2005 eruption, though we have no data to confirm this. Although subsidence during the 2005 eruption was not as great as during the 2018 eruption, the ~ 5 m subsidence is likely to have been sufficient to reduce the stress state in the edifice significantly.

After 5.8 m of uplift the increase in seismicity rate with total uplift slows, and then remains constant (apart from short-term fluctuations before and after large earthquakes described in Section 5.4) until the Mw 5.4 earthquake that triggered the eruption. The end of the exponential acceleration can be interpreted as the end of the “quasi-elastic” phase of Kilburn (2018), coming at the point that the differential stress reaches a critical failure value. Here, the ratio between the differential stress, S , and the critical or characteristic stress,

S_c , $S/S_c = \sim 5.8/1.1 = 5.1$ at the transition to inelastic behavior. For deformation in tension or extension, S_c is the tensile strength, σ_T , and, from the Mohr-Coulomb-Griffiths theory of failure, S / σ_T at the onset of failure (inelastic regime) is expected to be less than about 4 in tension and between 4 and 5.5 in compression. Thus, our value is slightly higher than the value of ~ 4 for tensile failure expected by Kilburn (2018). It is, however, consistent with the range of values expected for failure in compression, perhaps more aligned with the predominant thrust component of preeruptive earthquakes (Bell et al., 2021). One alternative explanation for the elevated value of this ratio at Sierra Negra is that the total uplift does not accurately represent the stress state of the edifice. It is possible that some amount of reinflation was required after the 2005 coeruptive deflation to return the TDF to a neutral stress state. We speculate that processes such as pore pressure changes or roof compression might be acting during this recovery phase, or, perhaps, visco-elastic processes relaxed the stress state on the trapdoor fault through the inflationary episode (Gregg et al., 2018).

The constant earthquake rate observed after the end of the exponential increase is consistent with the “steady inelastic” phase in the model of Kilburn (2018). Kilburn (2018) suggests this phase may be due to fault coalescence being inhibited by stress barriers. At Sierra Negra, the start of the steady earthquake rate phase approximately coincided with the onset of $M > 4$ earthquakes, which lower the stress on the TDF and temporarily suppress seismicity. It is likely that these earthquakes limit the increase in stress on the TDF, and prevent further increases in seismicity rate. There was no hyperbolic acceleration in earthquake rates prior to the eruption onset. A swarm of earthquakes initiated on the TDF eight hours after the Mw5.4 earthquake, most likely driven by dyke propagation within the TDF system. This earthquake was sufficiently large to perturb the stress field near the sill margins, promoting failure, and magma migration.

6.2. Evolution of Earthquake Magnitudes

The maximum-likelihood estimate of the b -value of the Gutenberg-Richter relation decreases systematically with total uplift before the 2018 eruption, reflecting an increase in the proportion of large earthquakes, and returns to a high value when inflation resumes after the end of the 2018 eruption. Apart from during the immediate onset of the eruption on June 26 (Bell et al., 2021), there is no evidence that the spatial distribution of seismicity changes with time. Therefore, it is most likely that this change reflects a temporal change in the properties of seismicity on the trapdoor fault system.

Although volcanic regions are often thought to be associated with b -values greater than one, these are often not well constrained, and a wide range of values have been reported (Roberts et al., 2015). In the laboratory, b -values are thought to reflect material heterogeneity or stress intensity, with lower b -values observed for higher stress intensities (Main et al., 1992; Sammonds et al., 1992). In tectonic regions, lower b -values are associated with thrust faulting, and accordingly higher differential stress (Schorlemmer et al., 2005). Few studies outside the laboratory document changes in b -value with stress through time within a single system. We argue that the decrease in the b -value before the 2018 eruption reflects the progressive increase in stress intensity on the fault system. The overall stress falls during deflation, and is low on return to inflation in late 2018. During the reinitiation of inflation, the b -value is higher, consistent with that reduced stress state.

The apparent change in b -value may also be explained, at least partly, by an evolution of the form of the magnitude-frequency distribution. Separating these two factors is challenging. However, the systematic change in the form of the magnitude-frequency distribution through many independent samples does suggest that this is a real effect. If so, this change is that expected for a transition from subcritical to critical conditions (Main, 1996), and consistent with the change from quasi-elastic to inelastic regimes (Kilburn, 2018).

6.3. Quiescence Following Larger Earthquakes

In the later stages of inflation, large earthquakes are followed by a period of seismic quiescence. This behavior is similar to that seen during caldera collapse events at Kilauea (Fildes et al., 2020; Shelly & Thelen, 2019) and Bárðarbunga (Gudmundsson et al., 2016), and in laboratory earthquake simulations (McLaskey, 2019; Passelègue et al., 2017), but to our knowledge is the first time it has been seen during preeruptive

inflation. It contrasts with the “mainshock-aftershock” type behavior typical of purely tectonic settings. This behavior suggests that these earthquakes reduce the overall stress state of the trapdoor fault, rather than simply redistributing it on to other parts of the system. However, we note that they do not slow the overall rate of uplift (Bell et al., 2021).

Surface ruptures were observed in the field associated with movement during the Mw5.4 earthquake. It is likely that the larger earthquakes in the months before the June 26 earthquake ruptured into the very weak upper rocks in the caldera, allowing the overall stress to drop, and perhaps preventing seismicity rates increasing further. Such large ruptures do indicate that the stress distribution is homogenized across large parts of the fault system. It is not clear whether the Mw5.4 earthquake that triggered the eruption occurred as the culmination of continued stress organization, or was a random realization of what was by then a steady-state process.

6.4. Implications for Deformation Processes

Pressure changes in the shallow magma chamber at Sierra Negra change the stress regime across the upper part of the volcanic edifice and trapdoor fault system. It is relaxed at the end of the 2005 eruption, highly stressed prior to the onset of the 2018 eruption, and then relaxed again at the end of the 2018 eruption. In addition, $M > 4$ earthquakes are sufficiently large that they temporarily drop the differential stress on a large enough section of the trapdoor fault system that it is noticeable in the total earthquake rates. Although the elastic-brittle processes controlling deformation are the same, the temporal evolution from what appears to be a subcritical state, through to a near critical one, and back to subcritical, differs from most tectonic environments. It shares more similarity with laboratory rock deformation experiments, where accelerating acoustic emission rates (Main et al., 1992) and reducing b -values (Sammonds et al., 1992) are commonly observed with increasing stress.

7. Conclusions

Fifteen years of surface uplift and seismicity data at Sierra Negra offer new insights into the nature of crustal deformation processes, and the properties of precursors to volcanic eruption. In this time, the surface of the caldera uplifted by 6.5 m during 13 years of inflation before the 2018 eruption. These intervals contain some of the highest amplitudes and rates of inflationary deformation ever recorded at a volcano. Rates of uplift and seismicity varied in time, in response to a variable supply of magma from depth to a shallow reservoir. However, the numbers of earthquakes per unit of uplift increased exponentially, and the b -value decreased, with total uplift, reflecting an increase in the differential stress on an intracaldera fault system. After ~ 5.8 m uplift, the fault system became critically stressed, and seismicity rates no longer increased. At this time, a sequence of $M > 4$ earthquakes was each followed by 2–3 days of seismic quiescence whilst the stress on the fault system recovered. The final and largest of these earthquakes changed the stress field on the shallow sill sufficiently to trigger failure, and the initiation of the eruption. After 8.5 m of subsidence during 2 months of co-eruptive deflation, the volcano began to re-inflate, and continues to do so at the time of writing. The drop in stress was accompanied by a return to low rates of seismicity (per unit uplift), and a recovery of a high b -value. Seismicity rates therefore reflect both the stress state of the fault system, and the local (in time) stressing rate. Analysis of both geodetic and seismic data is therefore critical to understanding the unrest state at deforming volcanoes.

Data Availability Statement

The earthquake catalog and processed uplift time series are archived in a Zenodo repository, 10.5281/zenodo.4984161. Raw seismic data are available from the Incorporated Research Institutions for Seismology (IRIS), Data services; <https://ds.iris.edu/> and from the IGPEN at <https://www.igpen.edu.ec/datos-mseed>. All geodetic data are available through the UNAVCO archive: <https://www.unavco.org/data/data.html>

Acknowledgments

The authors thank the Instituto Geofísico de la Escuela Politécnica Nacional and the Galápagos National Park for help and support with field-work and data access. They thank two anonymous reviewers for constructive comments that significantly improved the manuscript, and Chris Bean for helpful input during writing. This material is based on services provided by the GAGE Facility, operated by UNAVCO, Inc., with support from the National Science Foundation and the National Aeronautics and Space Administration under NSF Cooperative Agreement EAR-1724794. Part of this work was funded by the NSF award EAR 1838373, the IGUANA NERC Urgency grant NE/S002685/1.

References

Acocella, V. (2007). Understanding caldera structure and development: An overview of analogue models compared to natural calderas. *Earth-Science Reviews*, 85(3–4), 125–160. <https://doi.org/10.1016/j.earscirev.2007.08.004>

Aki, K. (1965). Maximum likelihood estimate of b in the formula $\log N = a - bM$ and its confidence limits. *Bulletin of the Earthquake Research Institute*, 43, 237–239.

Alvarado, A., Ruiz, M., Mothes, P., Yepes, H., Segovia, M., Vaca, M., et al. (2018). Seismic, volcanic, and geodetic networks in Ecuador: Building capacity for monitoring and research. *Seismological Research Letters*, 89(2A), 432–439. <https://doi.org/10.1785/0220170229>

Amelung, F., Jónsson, S., Zebker, H., & Segall, P. (2000). Widespread uplift and “trapdoor” faulting on Galapagos volcanoes observed with radar interferometry. *Nature*, 407(6807), 993–996. <https://doi.org/10.1038/35039604>

Anderson, J. G. (1979). Estimating the seismicity from geological structure for seismic-risk studies. *Bulletin of the Seismological Society of America*, 69(1), 135–158.

Bagnardi, M., & Amelung, F. (2012). Space-geodetic evidence for multiple magma reservoirs and subvolcanic lateral intrusions at Fernandina volcano, Galápagos Islands. *Journal of Geophysical Research*, 117, B10406. <https://doi.org/10.1029/2012JB009465>

Bell, A. F. (2018). Predictability of landslide timing from quasi-periodic precursory earthquakes. *Geophysical Research Letters*, 45, 1860–1869. <https://doi.org/10.1002/2017GL076730>

Bell, A. F., & Kilburn, C. R. J. (2012). Precursors to dyke-fed eruptions at basaltic volcanoes: Insights from patterns of volcano-tectonic seismicity at Kilauea volcano, Hawaii. *Bulletin of Volcanology*, 74(2), 325–339. <https://doi.org/10.1007/s00445-011-0519-3>

Bell, A. F., La Femina, P. C., Ruiz, M., Amelung, F., Bagnardi, M., Bean, C. J., et al. (2021). Caldera resurgence during the 2018 eruption of Sierra Negra volcano, Galápagos Islands. *Nature Communications*, 12(1), 1397. <https://doi.org/10.1038/s41467-021-21596-4>

Bell, A. F., Naylor, M., Hernandez, S., Main, I. G., Gaunt, H. E., Mothes, P., & Ruiz, M. (2018). Volcanic eruption forecasts from accelerating rates of drumbeat long-period earthquakes. *Geophysical Research Letters*, 45, 1339–1348. <https://doi.org/10.1002/2017GL076429>

Bertiger, W., Desai, S. D., Haines, B., Harvey, N., Moore, A. W., Owen, S., & Weiss, J. P. (2010). Single receiver phase ambiguity resolution with GPS data. *Journal of Geodesy*, 84(5), 327–337. <https://doi.org/10.1007/s00190-010-0371-9>

Biggs, J., Mothes, P. A., Ruiz, M. C., Amelung, F., Dixon, T. H., Baker, S., & Hong, S. H. (2010). Stratovolcano growth by co-eruptive intrusion: The 2008 eruption of Tungurahua Ecuador. *Geophysical Research Letters*, 37, L21302. <https://doi.org/10.1029/2010GL044942>

Björnsson, A., Johnsen, G., Sigurdsson, S., Thorbergsson, G., & Tryggvason, E. (1979). Rifting of the plate boundary in north Iceland 1975–1978. *Journal of Geophysical Research*, 84(B6), 3029. <https://doi.org/10.1029/JB084iB06p03029>

Blake, S., & Cortés, J. A. (2018). Forecasting deflation, intrusion and eruption at inflating volcanoes. *Earth and Planetary Science Letters*, 481, 246–254. <https://doi.org/10.1016/j.epsl.2017.10.040>

Boehm, J., Werl, B., & Schuh, H. (2006). Troposphere mapping functions for GPS and very long baseline interferometry from European centre for medium-range weather forecasts operational analysis data. *Journal of Geophysical Research*, 111, B02406. <https://doi.org/10.1029/2005JB003629>

Chadwick, W. W., Geist, D. J., Jónsson, S., Poland, M., Johnson, D. J., & Meertens, C. M. (2006). A volcano bursting at the seams: Inflation, faulting, and eruption at Sierra Negra volcano, Galápagos. *Geology*, 34(12), 1025. <https://doi.org/10.1130/G22826A.1>

Cullen, A. B., McBirney, A. R., & Rogers, R. D. (1987). Structural controls on the morphology of Galapagos shields. *Journal of Volcanology and Geothermal Research*, 34(1–2), 143–151. [https://doi.org/10.1016/0377-0273\(87\)90099-0](https://doi.org/10.1016/0377-0273(87)90099-0)

Fildes, R. A., Kellogg, L. H., Turcotte, D. L., & Rundle, J. B. (2020). Interevent seismicity statistics associated with the 2018 quasiperiodic collapse events at Kilauea, HI, USA. *Earth and Space Science*, 7, e2019EA000766. <https://doi.org/10.1029/2019EA000766>

Filson, J., Simkin, T., & Leu, L. (1973). Seismicity of a caldera collapse: Galapagos Islands 1968. *Journal of Geophysical Research*, 78(35), 8591–8622. <https://doi.org/10.1029/JB078i035p08591>

Galetto, F., Bagnardi, M., Acocella, V., & Hooper, A. (2019). Non-eruptive unrest at the caldera of Alcedo volcano (Galápagos Islands) revealed by InSAR data and geodetic modelling. *Journal of Geophysical Research: Solid Earth*, 124, 3365–3381. <https://doi.org/10.1029/2018JB017103>

Geist, D. J., Harpp, K. S., Naumann, T. R., Poland, M., Chadwick, W. W., Hall, M., & Rader, E. (2008). The 2005 eruption of Sierra Negra volcano, Galápagos, Ecuador. *Bulletin of Volcanology*, 70(6), 655–673. <https://doi.org/10.1007/s00445-007-0160-3>

Gregg, P. M., Le Mével, H., Zhan, Y., Dufek, J., Geist, D., & Chadwick, W. W. (2018). Stress triggering of the 2005 eruption of Sierra Negra volcano, Galápagos. *Geophysical Research Letters*, 45, 13288–13297. <https://doi.org/10.1029/2018GL080393>

Gudmundsson, A. (2012). Magma chambers: Formation, local stresses, excess pressures, and compartments. *Journal of Volcanology and Geothermal Research*, 237–238, 19–41. <https://doi.org/10.1016/j.jvolgeores.2012.05.015>

Gudmundsson, M. T., Jónsdóttir, K., Hooper, A., Holohan, E. P., Halldórsson, S. A., Ófeigsson, B. G., et al. (2016). Gradual caldera collapse at Bárðarbunga volcano, Iceland, regulated by lateral magma outflow. *Science*, 353(6296), aaf8988. <https://doi.org/10.1126/science.aaf8988>

Gutenberg, B., & Richter, C. F. (1954). *Seismicity of the Earth* (2nd ed.). Geological Society of America.

Harpp, K. S., & Geist, D. J. (2018). The evolution of Galápagos volcanoes: An alternative perspective. *Frontiers in Earth Science*, 6, 50. <https://doi.org/10.3389/feart.2018.00050>

Jónsson, S. (2009). Stress interaction between magma accumulation and trapdoor faulting on Sierra Negra volcano, Galápagos. *Tectonophysics*, 471(1–2), 36–44. <https://doi.org/10.1016/j.tecto.2008.08.005>

Jónsson, S., Zebker, H., & Amelung, F. (2005). On trapdoor faulting at Sierra Negra volcano, Galápagos. *Journal of Volcanology and Geothermal Research*, 144(1–4), 59–71. <https://doi.org/10.1016/j.jvolgeores.2004.11.029>

Kanamori, H. (1977). The energy release in great earthquakes. *Journal of Geophysical Research*, 82(20), 2981–2987. <https://doi.org/10.1029/JB082i020p02981>

Kilburn, C. R. J. (2003). Multiscale fracturing as a key to forecasting volcanic eruptions. *Journal of Volcanology and Geothermal Research*, 125(3–4), 271–289. [https://doi.org/10.1016/S0377-0273\(03\)00117-3](https://doi.org/10.1016/S0377-0273(03)00117-3)

Kilburn, C. R. J. (2018). Forecasting volcanic eruptions: Beyond the failure forecast method. *Frontiers in Earth Science*, 6, 133. <https://doi.org/10.3389/feart.2018.00133>

Kilburn, C. R. J., De Natale, G., & Carlino, S. (2017). Progressive approach to eruption at Campi Flegrei caldera in southern Italy. *Nature Communications*, 8, 15312. <https://doi.org/10.1038/ncomms15312>

Kilburn, C. R. J., & Voight, B. (1998). Slow rock fracture as eruption precursor at Soufriere Hills Volcano, Montserrat. *Geophysical Research Letters*, 25(19), 3665–3668. <https://doi.org/10.1029/98GL01609>

Krischer, L., Megies, T., Barsch, R., Beyreuther, M., Lecocq, T., Caudron, C., & Wassermann, J. (2015). ObsPy: A bridge for seismology into the scientific Python ecosystem. *Computational Science and Discovery*, 8(1), 014003. <https://doi.org/10.1088/1749-4699/8/1/014003>

- Larson, K. M., & Miyazaki, S. (2008). Resolving static offsets from high-rate GPS data: The 2003 Tokachi-oki earthquake. *Earth, Planets and Space*, 60(8), 801–808. <https://doi.org/10.1186/BF03352831>
- Lyard, F., Lefevre, F., Letellier, T., & Francis, O. (2006). Modelling the global ocean tides: Modern insights from FES2004. *Ocean Dynamics*, 56(5–6), 394–415. <https://doi.org/10.1007/s10236-006-0086-x>
- Main, I. G. (1996). Statistical physics, seismogenesis, and seismic hazard. *Reviews of Geophysics*, 34(4), 433–462. <https://doi.org/10.1029/96RG02808>
- Main, I. G., Meredith, P. G., & Sammonds, P. R. (1992). Temporal variations in seismic event rate and b-values from stress corrosion constitutive laws. *Tectonophysics*, 211(1–4), 233–246. [https://doi.org/10.1016/0040-1951\(92\)90061-A](https://doi.org/10.1016/0040-1951(92)90061-A)
- McLaskey, G. C. (2019). Earthquake initiation from laboratory observations and implications for foreshocks. *Journal of Geophysical Research: Solid Earth*, 124, 12882–12904. <https://doi.org/10.1029/2019JB018363>
- Nooner, S. L., & Chadwick, W. W. (2016). Inflation-predictable behavior and co-eruption deformation at Axial Seamount. *Science*, 354(6318), 1399–1403. <https://doi.org/10.1126/science.aah4666>
- Pancha, A., Anderson, J. G., & Kreemer, C. (2006). Comparison of seismic and geodetic scalar moment rates across the basin and range province. *Bulletin of the Seismological Society of America*, 96(1), 11–32. <https://doi.org/10.1785/0120040166>
- Passelègue, F. X., Latour, S., Schubnel, A., Nielsen, S., Bhat, H. S., & Madariaga, R. (2017). Influence of fault strength on precursory processes during laboratory earthquakes. In M. Y. Thomas, T. M. Mitchell, & H. S. Bhat (Eds.), *Fault zone dynamic processes* (pp. 229–242). AGU. <https://doi.org/10.1002/9781119156895.ch12>
- Poland, M. P. (2014). Contrasting volcanism in Hawai'i and the Galápagos. In K. S. Harpp, E. Mittelstaedt, N. D'Ozouville, & D. W. Graham (Eds.), *The Galápagos: A natural laboratory for the Earth sciences* (Vol. 204, pp. 5–26). Washington, DC: American Geophysical Union. <https://doi.org/10.1002/9781118852538.ch2>
- Reischung, P., Griffiths, J., Ray, J., Schmid, R., Collilieux, X., & Garayt, B. (2012). IGS08: The IGS realization of ITRF2008. *GPS Solutions*, 16(4), 483–494. <https://doi.org/10.1007/s10291-011-0248-2>
- Roberts, N. S., Bell, A. F., & Main, I. G. (2015). Are volcanic seismic b-values high, and if so when? *Journal of Volcanology and Geothermal Research*, 308, 127–141. <https://doi.org/10.1016/j.jvolgeores.2015.10.021>
- Robertson, R. M., & Kilburn, C. R. J. (2016). Deformation regime and long-term precursors to eruption at large calderas: Rabaul, Papua New Guinea. *Earth and Planetary Science Letters*, 438, 86–94. <https://doi.org/10.1016/j.epsl.2016.01.003>
- Roman, D. C., & Cashman, K. V. (2006). The origin of volcano-tectonic earthquake swarms. *Geology*, 34(6), 457–460. <https://doi.org/10.1130/G22269.1>
- Rundle, J. B., Turcotte, D. L., Shcherbakov, R., Klein, W., & Sammis, C. (2003). Statistical physics approach to understanding the multiscale dynamics of earthquake fault systems. *Reviews of Geophysics*, 41(4), 1019. <https://doi.org/10.1029/2003RG000135>
- Salvatier, J., Wiecki, T. V., & Fonnesbeck, C. (2016). Probabilistic programming in Python using PyMC3. *PeerJ Computer Science*, 2, e55. <https://doi.org/10.7717/peerj-cs.55>
- Sammonds, P. R., Meredith, P. G., & Main, I. G. (1992). Role of pore fluids in the generation of seismic precursors to shear fracture. *Nature*, 359(6392), 228–230. <https://doi.org/10.1038/359228a0>
- Schorlemmer, D., Wiemer, S., & Wyss, M. (2005). Variations in earthquake-size distribution across different stress regimes. *Nature*, 437(7058), 539–542. <https://doi.org/10.1038/nature04094>
- Shelly, D. R., & Thelen, W. A. (2019). Anatomy of a caldera collapse: Kilauea 2018 summit seismicity sequence in high resolution. *Geophysical Research Letters*, 46, 14395–14403. <https://doi.org/10.1029/2019GL085636>
- Simkin, T., & Howard, K. A. (1970). Caldera collapse in the Galapagos Islands, 1968. *Science*, 169(3944), 429–437. <https://doi.org/10.1126/science.169.3944.429>
- Sparks, R. S. J. (2003). Forecasting volcanic eruptions. *Earth and Planetary Science Letters*, 210(1–2), 1–15. [https://doi.org/10.1016/S0012-821X\(03\)00124-9](https://doi.org/10.1016/S0012-821X(03)00124-9)
- Squires, D. (1979). Report on Sierra Negra (Ecuador). *Scientific Event Alert Network Bulletin*, 4(12). <https://doi.org/10.5479/si.GVP.SEAN197912-353050>
- Tepp, G., Ebinger, C. J., Ruiz, M., & Belachew, M. (2014). Imaging rapidly deforming ocean island volcanoes in the western Galápagos archipelago, Ecuador. *Journal of Geophysical Research: Solid Earth*, 119, 442–463. <https://doi.org/10.1002/2013JB010227>
- Tilling, R. I., & Dvorak, J. J. (1993). Anatomy of a basaltic volcano. *Nature*, 363, 125–133. <https://doi.org/10.1038/363125a0>
- Vasconez, F., Ramón, P., Hernandez, S., Hidalgo, S., Bernard, B., Ruiz, M., et al. (2018). The different characteristics of the recent eruptions of Fernandina and Sierra Negra volcanoes (Galápagos, Ecuador). *Volcanica*, 1(2), 127–133. <https://doi.org/10.30909/vol.01.02.127133>
- Voight, B. (1988). A method for prediction of volcanic eruptions. *Nature*, 332(6160), 125–130. <https://doi.org/10.1038/332125a0>
- Voight, B. (1989). A relation to describe rate-dependent material failure. *Science*, 243(4888), 200–203. <https://doi.org/10.1126/science.243.4888.200>
- White, R. A., & McCausland, W. A. (2019). A process-based model of pre-eruption seismicity patterns and its use for eruption forecasting at dormant stratovolcanoes. *Journal of Volcanology and Geothermal Research*, 382, 267–297. <https://doi.org/10.1016/j.jvolgeores.2019.03.004>
- Yun, S., Segall, P., & Zebker, H. (2006). Constraints on magma chamber geometry at Sierra Negra volcano, Galápagos Islands, based on InSAR observations. *Journal of Volcanology and Geothermal Research*, 150(1–3), 232–243. <https://doi.org/10.1016/j.jvolgeores.2005.07.009>
- Zumberge, J. F., Heflin, M. B., Jefferson, D. C., Watkins, M. M., & Webb, F. H. (1997). Precise point positioning for the efficient and robust analysis of GPS data from large networks. *Journal of Geophysical Research*, 102(B3), 5005–5017. <https://doi.org/10.1029/96JB03860>